JACS
JOURNAL OF THE AMERICAN CHEMICAL SOCIETY



Article

# Biodegradation-Mediated Enzymatic Activity-Tunable Molybdenum Oxide Nanourchins for Tumor-Specific Cascade Catalytic Therapy

Xi Hu, Fangyuan Li, Fan Xia, Xia Guo, Nan Wang, Lili Liang, Bo Yang, Kelong Fan, Xiyun Yan, and Daishun Ling

*J. Am. Chem. Soc.*, **Just Accepted Manuscript** • DOI: 10.1021/jacs.9b13586 • Publication Date (Web): 27 Dec 2019



## Just Accepted



is published by the American Chemical Society. 1155 Sixteenth Street N.W., Washington, DC 20036

# Biodegradation-Mediated Enzymatic Activity-Tunable Molybdenum Oxide Nanourchins for Tumor-Specific Cascade Catalytic Therapy

Xi Hu,[†,‡,§,o,#,⊥] Fangyuan Li,[†,‡,§,⊥] Fan Xia,[†,‡,⊥] Xia Guo,[†,‡] Nan Wang,[†] Lili Liang,[†] Bo Yang,[‡] Kelong Fan,[Δ,∇] Xiyun Yan,[Δ,∇] Daishun Ling*[,†,‡,§,o]

[†] Institute of Pharmaceutics, College of Pharmaceutical Sciences, Zhejiang University, Hangzhou 310058, China

[‡] Zhejiang Province Key Laboratory of Anti-Cancer Drug Research, College of Pharmaceutical Sciences, Zhejiang University, Hangzhou 310058, China

[§] Hangzhou Institute of Innovative Medicine, College of Pharmaceutical Sciences, Zhejiang University, Hangzhou 310058, China

[o] Key Laboratory of Biomedical Engineering of the Ministry of Education, College of Biomedical Engineering & Instrument Science, Zhejiang University, Hangzhou 310058, China

[#] The First Affiliated Hospital, College of Medicine, Zhejiang University, Hangzhou 310003, China

[Δ] CAS Engineering Laboratory for Nanozyme, Key Laboratory of Protein and Peptide Pharmaceutical, Institute of Biophysics, Chinese Academy of Sciences, 15 Datun Road, Beijing 100101, China

[∇] Academy of Medical Sciences, Zhengzhou University, 40 N Daxue Road, Zhengzhou 450052, China

**ABSTRACT:** Recent advances in nanomedicine have facilitated the development of potent nanomaterials with intrinsic enzyme-like activities (nanozymes) for cancer therapy. However, it remains great challenges to fabricate smart nanozymes that precisely perform enzymatic activity in tumor microenvironment without inducing off-target toxicity to surrounding normal tissues. Herein, we report on designed fabrication of biodegradation-medicated enzymatic activity-tunable molybdenum oxide nanourchins ($MoO_{3-x}$ NUs), which selectively perform therapeutic activity in tumor microenvironment via cascade catalytic reactions, while keep normal tissues unharmed due to their responsive biodegradation in physiological environment. Specifically, the $MoO_{3-x}$ NUs first induce catalase (CAT)-like reactivity to decompose hydrogen peroxide ($H_2O_2$) in tumor microenvironment, producing a considerable amount of $O_2$ for subsequent oxidase (OXD)-like reactivity of $MoO_{3-x}$ NUs; a substantial cytotoxic superoxide radical ($^{\cdot}O_2^-$) is thus generated for tumor cell apoptosis. Interestingly, once exposed upon neutral blood or normal tissues, $MoO_{3-x}$ NUs rapidly lose the enzymatic activity via pH-responsive biodegradation and are excreted in urine, thus ultimately ensuring safety. The current study demonstrates a proof of concept of biodegradation-medicated in vivo catalytic activity tunable nanozymes for tumor specific cascade catalytic therapy with minimal off-target toxicity.

## INTRODUCTION

Chemically-engineered functional nanomaterials with intrinsic biological activities, exerting potent anti-cancer therapeutic effects via, e.g., generation of reactive oxygen species (ROS),[1-6] selective ion leaching,[7,8] or radiosensitizing effects,[9] represent a new era of cancer nanomedicines. In particular, nanomaterials mimicking oxidoreductase including peroxidase (POD), oxidase (OXD), and catalase (CAT), so called "Nanozyme", have sparked an increasing interest because they can fine-tune the intracellular biochemical reactions for satisfactory tumor diagnostic and/or therapeutic outcomes.[1,10-18] However, for in vivo applications, the undesired off-target activity of nanozyme can lead to unpredictable toxicity.[1,19,20] Hence, it is highly desirable to confine the catalytic reaction-based therapeutic effects of nanozymes exclusively in tumors, while being inert to normal tissues, which is extremely valuable but yet remains a significant challenge.

In nature, the activities of biological enzymes are correlated with their defined structures.[21,22] For instance, the enzymatic effect of the antiretroviral enzyme APOBEC3G for viral cDNA replication can be suppressed once they are degraded by the proteasome.[23] We are, therefore, inspired to explore the on/off-switchable activity of nanozymes via the biodegradation-mediated regulation of their nanostructures. It is reported that the branched nanomaterials own large population of atoms at their corners and edges, thus gaining large active surface area with high reactivity.[24-26] For example, $Mn_3O_4$ nanoflowers exhibit much higher CAT-, glutathione

**Scheme 1. Schematic illustration of biodegradation-medicated enzymatic activity-tunable molybdenum oxide nanourchins ($MoO_{3-x}$ NUs) with the highly specific toxicity to tumor tissues via a multi-enzyme stepwise cascade catalysis in acidic tumor microenvironment, while leaving normal tissues unharmed due to their pH-responsive biodegradation and subsequent renal excretion in physiological environment.**

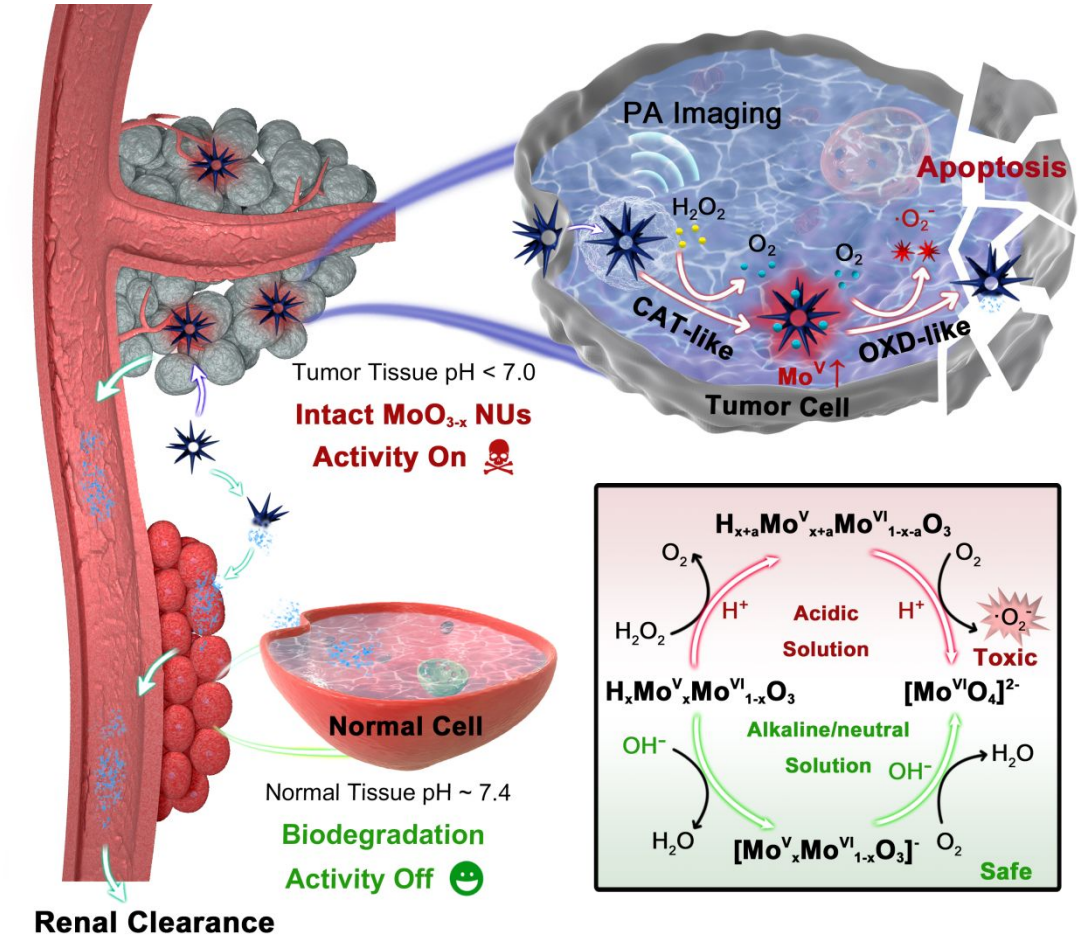


peroxidase (GPx)-, and superoxide dismutase (SOD)-like catalytic activities than other shaped $Mn_3O_4$ nanomaterials (e.g., flakes, cubes, polyhedra, and hexagonal plates).[27] In this consideration, we envision that the dynamic biodegradation-mediated structural regulation of nanozymes between pathological and physiological conditions can hopefully achieve the concurrent tumor selective catalytic therapy and great biocompatibility with surrounding normal tissues.

Herein, we report for the first time that $MoO_{3-x}$ nanourchins (NUs) with a structure-dependent enzymatic activity can perform highly specific cascade catalytic activity exclusively against tumor, while leaving normal tissues unharmed due to their rapid biodegradation in physiological environment. In our design, benefiting from the large active surface area and high proportion of active $Mo^V$ atoms, $MoO_{3-x}$ NUs reveal the excellent CAT-like activity in acidic tumor microenvironment, generating abundant $O_2$ via decomposing $H_2O_2$; and subsequently, the OXD-like activity of $MoO_{3-x}$ NUs is activated to transfer electrons to $O_2$ and form cytotoxic superoxide radicals ($^{\bullet}O_2^-$) (Scheme 1). However, on exposure to a physiological environment (pH~7.4), $MoO_{3-x}$ NUs would rapidly lose the enzymatic activity via the pH-responsive biodegradation, whose products are proved to be renal clearable and biocompatible molybdate ions.

## RESULTS AND DISCUSSION

**Synthesis and Characterization of $MoO_{3-x}$ NUs.** Initially, spherical $MoO_{3-x}$ nanoparticles were synthesized via uniformly heating of the reactants at 100 ˚C (Figure S1). Then, the $MoO_{3-x}$ NUs were obtained after a solvothermal reaction at 160 ˚C (Figure 1a). As revealed by transmission microscopy (TEM), the NUs are hollow and covered with spikes (Figures 1b and S2). The average core size of the NUs is 142.8±13.3 nm, and the surface spikes are 15.4±3.3 nm in cross-sectional diameter and 116.7±24.6 nm in length (Nano Measure Software). As identified by X-ray diffraction (XRD) analysis, the $MoO_{3-x}$ NUs are primarily composed of hexagonal $MoO_{3-x}$ (PDF no. 21-0569; Figure S3). Besides, Mo 3d X-ray photoelectron spectroscopy (XPS) spectrum reveals the presence of $Mo^{VI}$ species (BE at 235.8 eV and 232.6 eV) and $Mo^V$ (BE at 234.3 eV and 231.5 eV),[28-30] and the proportion of $Mo^V$ species in $MoO_{3-x}$ NUs is calculated to be ~47.0% (Figure 1c). Furthermore, the Raman spectrum demonstrates the existence of $H^+$ in $MoO_{3-x}$ NUs (Figure S4), indicating that the composition is $H_x(Mo^V_x)(Mo^{VI}_{1-x})O_3$ (x=0.47, abbreviated as $MoO_{3-x}$).[31-33] It

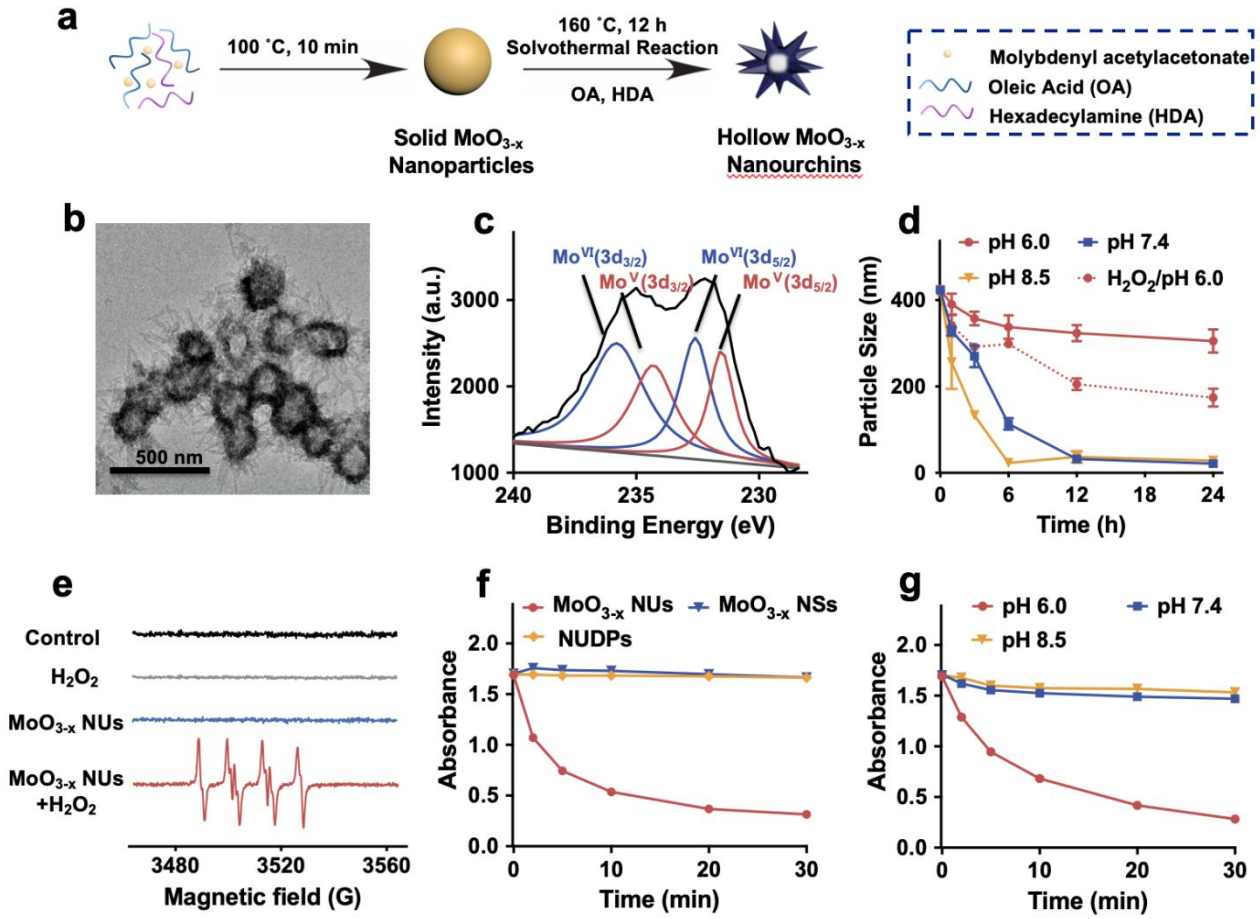


**Figure 1.** Synthesis and characterization of $MoO_{3-x}$ NUs. (a) Schematic illustration of the synthesis process of $MoO_{3-x}$ NUs. (b) The TEM image of $MoO_{3-x}$ NUs. (c) The Mo XPS spectrum of $MoO_{3-x}$ NUs. (d) Particle sizes of $MoO_{3-x}$ NUs at various time points after incubation in PBS (pH 6.0, pH 7.4, and pH 8.5), 1 mM $H_2O_2$/PBS (pH 6.0), and distilled water. (e) Electron spin resonance (ESR) spectra of $MoO_{3-x}$ NUs in the presence of BMPO and $H_2O_2$ (1 mM). (f) UV-Vis absorbance of 1,3-diphenylisobenzofuran (DPBF) in distilled water/ethanol solutions with $MoO_{3-x}$ NUs, $MoO_{3-x}$ nanosheets (NSs), or NUDPs (Mo, 20 μg; λ=410 nm). (g) UV-Vis absorbance of DPBF in PBS (pH 6.0, pH 7.4, and pH 8.5)/ethanol solutions with $MoO_{3-x}$ NUs (Mo, 20 μg; λ=410 nm).

is speculated that the etching process is originated from the central part with the assistant of oleic acid (OA) and hexadecylamine (HDA) as etching agents, accompanied by a reduction in the Mo species.[34,35]

**pH-Responsive Biodegradation of $MoO_{3-x}$ NUs.** 1,2-distearoyl-sn-glycero-3-phosphoethanolamine-N-[methoxy (polyethylene glycol)-2000] (DSPE-$PEG_{2000}$) was employed for surface modification, as confirmed by thermogravimetric analysis (TGA) and Fourier transform infrared (FT-IR) spectra analysis (Figure S5). Moreover, $MoO_{3-x}$ NUs could be easily degraded in aqueous solution containing $H_2O_2$ or $OH^-$, accompanied by color fading (Figure S6). As shown in Figure 1d, the particle size of $MoO_{3-x}$ NUs decreases rapidly in both neutral and alkaline phosphate buffer saline (PBS). Interestingly, the size decrease is very slow under acidic conditions but can be accelerated with the added $H_2O_2$. Moreover, the Mo XPS spectrum of $MoO_{3-x}$ NUs degradation products (NUDPs) confirms the oxidation of $Mo^V$ species into $Mo^{VI}$ species (Figure S7).[36-38] Furthermore, the pH dependent Mo ion release profiles as measured by an inductively coupled plasma mass spectrometer (ICP-MS) are consistent with the trends of particle size changes as shown in Figure 1d, implying that the NUDPs should be molybdate ions (Figure S8). From the UV-Vis-NIR spectrum, $MoO_{3-x}$ NUs show a broad absorption band in the NIR region, which dramatically vanishes under the neutral, alkaline, and $H_2O_2$ conditions (Figure S9). According to the pH-responsive biodegradation, it is speculated that small ions such as $H^+$ are implanted into the urchin-like nanostructure, accompanied by the partial reduction of Mo species with the assistant of OA and HDA as etching agents.[31]

**Biodegradation Regulated Enzymatic Activity and Catalytic Mechanism of $MoO_{3-x}$ NUs.** We further investigated the enzyme-like activity of $MoO_{3-x}$ NUs. The gas bubbles and $O_2$ concentration profiles indicate that the $O_2$ production capability of $MoO_{3-x}$ NUs in acidic PBS is much stronger than that in neutral or alkaline PBS, demonstrating the decreased CAT-like activity of $MoO_{3-x}$ NUs induced by the pH-responsive biodegradation in neural and alkaline environments (Figure S10). Also, we found that o-phenylenediamine (OPD) and 3,3',5,5'-

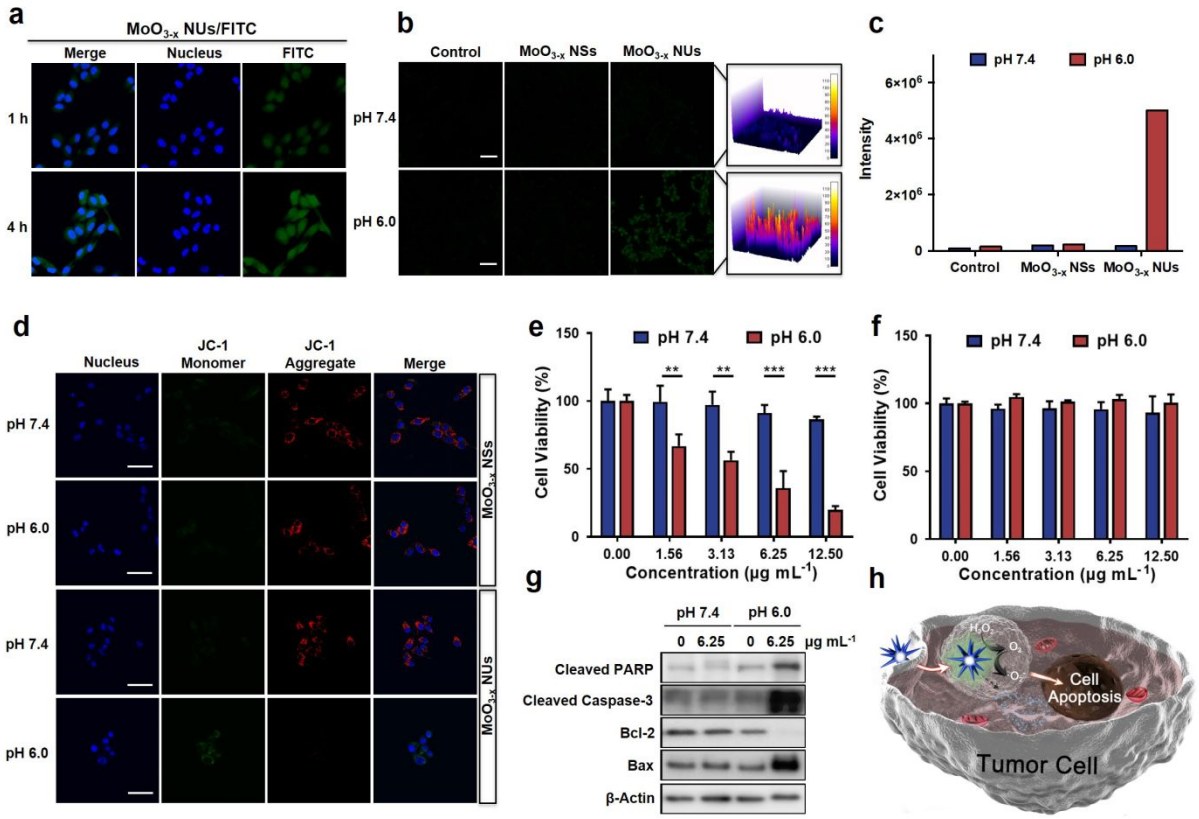


**Figure 2.** pH-Dependent cell death caused by $MoO_{3-x}$ NUs with biodegradation-regulated catalytic activity. (a) Representative confocal laser scanning microscopic (CLSM) images of B16 tumor cells after incubation with DMEM (pH 6.0) containing $MoO_{3-x}$ NUs/FITC for 1 h and 4 h. (b) Representative CLSM images of the degree of intracellular oxidative stress via DCFH-DA staining. Right panel, 3D mapping of intracellular fluorescence. Cells were treated with DMEM containing $MoO_{3-x}$ NUs or $MoO_{3-x}$ NSs (Mo, 6.25 μg $mL^{-1}$) at pH 7.4 and pH 6.0, respectively. Scale bar=100 μm. (c) Quantitative analysis of intracellular ROS fluorescence intensity. (d) Effect of $MoO_{3-x}$ NUs or $MoO_{3-x}$ NSs (Mo, 6.25 μg $mL^{-1}$) on mitochondrial membrane potential ($\Delta\psi_m$) in B16 cells. Red JC-1 aggregate indicates mitochondria with a normal membrane potential, and the green JC-1 monomer means the mitochondria with a depolarized membrane (impaired mitochondria). Scale bar=50 μm. (g) Effects of $MoO_{3-x}$ NUs on the expression of cleaved PARP, cleaved caspase-3, Bax, and Bcl-2. Cytotoxicity of $MoO_{3-x}$ NUs (e) or $MoO_{3-x}$ NSs (f) to B16 tumor cells after incubation in DMEM at pH 7.4 and pH 6.0. (h) Schematic illustration of $MoO_{3-x}$ NUs-induced anti-tumor mechanism. *P<0.05, **P<0.01, ***P<0.001.

tetramethylbenzidine (TMB) could be oxidized by $MoO_{3-x}$ NUs in the presence of $H_2O_2$ (Figure S11). To elucidate the catalytic mechanism of $MoO_{3-x}$ NUs, the type of free radical products was determined via electron spin resonance (ESR) with 5-tertbutoxycarbonyl-5methyl-1-pyrroline N-oxide (BMPO) as the specific spin trap reagent (Figure 1e), which shows that $^{\cdot}O_2^-$ is the unique product in the $MoO_{3-x}$ NUs-catalyzed reaction. These results indicate that $MoO_{3-x}$ NUs can efficiently yield $^{\cdot}O_2^-$, in sharp contrast to either NUDPs or $MoO_{3-x}$ nanosheets (NSs; Figure S12).[31] Moreover, 1,3-diphenylisobenzofuran (DPBF) and methylene blue (MB) were applied to further verify the ROS products of the reaction, and the ROS produced by $MoO_{3-x}$ NUs is verified to be $^{\cdot}O_2^-$ rather than $^1O_2$[39] or ·OH (Figures 1f, S13 and S14), indicating the OXD-like activity of $MoO_{3-x}$ NUs.[10,11] Moreover, it is noteworthy that the proper amount of $H_2O_2$ can increase the proportion of $Mo^V$ species on the surface of $MoO_{3-x}$ NUs (from 47.0% to 53.3%; Figures 1c and S15), enhancing the OXD-like activity of $MoO_{3-x}$ NUs (Scheme 1); while the over excess amount of $H_2O_2$ or long incubation time leads to the oxidization of $Mo^V$ species and consequently decrease the OXD-like activity of $MoO_{3-x}$ NUs (Figure S16). These results suggest that, $MoO_{3-x}$ NUs decompose the $H_2O_2$ into $O_2$ with the increasing of the proportion of $Mo^V$ species. Subsequently, the generated $O_2$ is easily adsorbed on the large active surface of $MoO_{3-x}$ NUs and being transformed into $^{\cdot}O_2^-$ by $Mo^V$ via the cascade reactions, revealing the activated OXD-like activity. The active electron for the "$O_2$–$^{\cdot}O_2^-$" reaction is probably derived from the intervalence charge-transfer transition between $Mo^V$ to $Mo^{VI}$ on the surface of $MoO_{3-x}$ NUs.[40-43] In contrast, no ROS product of $MoO_{3-x}$ NSs (containing 37% $Mo^V$ species)[31] was detected in the same procedure (Figures 1f, S12, S14 and S17). The high ROS production efficiency of $MoO_{3-x}$ NUs is likely attributed to their large active surface area and the high proportion of $Mo^V$ atoms exposed at the sites of surface defects.[26,44,45]

During the pH-responsive biodegradation process in neutral and alkaline environments, $Mo^V$ species of $MoO_{3-x}$ NUs are oxidized and depleted, resulting in the vanishment of the CAT-like and OXD-like activities (Figures 1f,g and S10, S18). Nevertheless, $MoO_{3-x}$ NUs maintain great enzymatic activity after storage in distilled water for 7 d

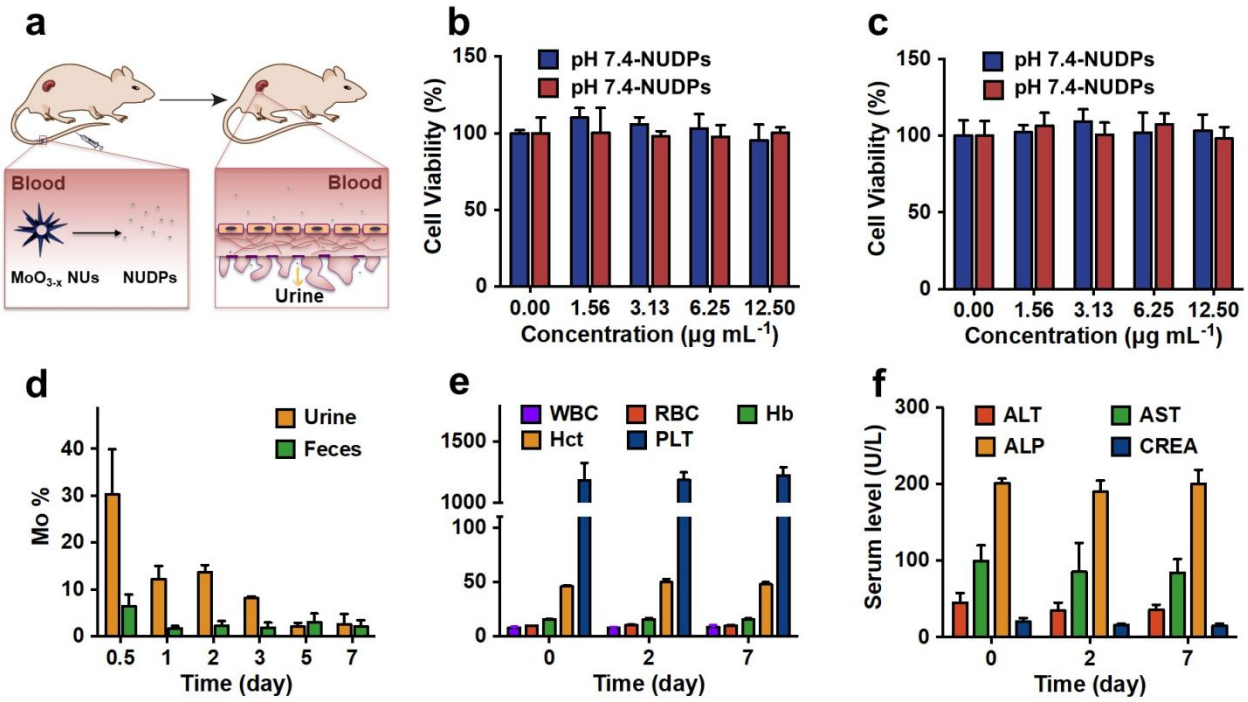


**Figure 3.** The safety evaluation of $MoO_{3-x}$ NUs after biodegradation once entering circulation system. (a) Illustration of the in vivo fate of $MoO_{3-x}$ NUs after intravenous administration. On exposure to neutral blood or normal tissues, $MoO_{3-x}$ NUs biodegrade into safe ions, which then are excreted via kidney, thus ensuring great biocompatibility. (b,c) Cytotoxicity of NUDPs to B16 tumor cells (b) and L02 normal cells (c) at pH 7.4 and pH 6.0. (d) Mo in urine and feces of mice at indicated time points after intravenous injection of $MoO_{3-x}$ NUs (n=6). (e) Hematology data, including white blood cells ($10^9$ L$^{-1}$, WBC), red blood cells ($10^{12}$ L$^{-1}$, RBC), hemoglobin (g L$^{-1}$, Hb), hematocrit (%, Hct), platelets ($10^9$ L$^{-1}$, PLT) of mice at 0 d, 2 d, and 7 d post intravenous injection with $MoO_{3-x}$ NUs (n=6). (f) Blood biochemical tests, including alanine aminotransferase (ALT), aspartate aminotransferase (AST), alkaline phosphatase (ALP), and creatinine (CREA) on mice at 0 d, 2 d, and 7 d post intravenous injection with $MoO_{3-x}$ NUs (n=6).

(Figure S19), and could be used for at least three cycles (Figure S20), indicating the stability and reusability of $MoO_{3-x}$ NUs.

**Biodegradation Regulated in Vitro Cytotoxicity and Cell Death Mechanism.** Firstly, the cellular uptake of both $MoO_{3-x}$ NUs and $MoO_{3-x}$ NSs was confirmed by confocal laser scanning microscopy (CLSM; Figures 2a and S21). As to enzyme-like $MoO_{3-x}$ NUs, they could effectively consume tumor intracellular high levels of $H_2O_2$[46] and yield excessive amounts of $^{\cdot}O_2^-$ to elicit irreversible biomolecules and membrane damage.[47-49] To further investigate the biodegradation regulated catalytic activity at the cellular levels, following cellular studies including ROS levels, mitochondrial membrane potential, cytotoxicity, and apoptosis, were conducted at both acidic condition (pH 6.0) and neutral condition (pH 7.4). The tumor cells incubated with $MoO_{3-x}$ NUs or $MoO_{3-x}$ NSs were stained with 2,7-dichlorofluorescin diacetate (DCFH-DA) to visualize the intracellular ROS levels (Figure 2b,c). Interestingly, the fluorescence intensity of $MoO_{3-x}$ NUs-treated cells increases sharply with a reduction in pH because the $^{\cdot}O_2^-$ is the primary product at acidic pH; while the $^{\cdot}O_2^-$ generation pathway is blocked at a neutral pH owing to the rapid oxidative biodegradation of $MoO_{3-x}$ NUs (Scheme 1). Also, cells treated with $MoO_{3-x}$ NUs at pH 6.0 reveal markedly higher intracellular ROS levels than those treated with $MoO_{3-x}$ NSs. Moreover, JC-1 staining analysis shows that the excess generation of $^{\cdot}O_2^-$ by $MoO_{3-x}$ NUs in an acidic environment impacts the mitochondrial membrane potential ($\Delta\psi_m$) and leads to mitochondrial membrane disruption (Figure 2d). Consequently, the $MoO_{3-x}$ NUs exhibit significant cytotoxicity in acidic media, while no obvious cell death is observed in neutral media (Figure 2e). In contrast, there is negligible cytotoxicity of $MoO_{3-x}$ NSs to tumor cells (Figure 2f), indicating the superior cytotoxicity of $MoO_{3-x}$ NUs is based on their unique morphology as well as abundant $Mo^V$ species. Furthermore, western blot analysis was performed to verify the expression of anti-apoptotic and apoptotic proteins in tumor cells upon exposure to $MoO_{3-x}$ NUs (Figure 2g) or $MoO_{3-x}$ NSs (Figure S22). The expression levels of cleaved PARP, cleaved caspase-3 as well as the Bax/Bcl-2 ratio significantly increase in B16 tumor cells incubated in DMEM at pH 6.0. Taken together, we can conclude that once internalized in acidic lysosomes of tumor cells, the $MoO_{3-x}$ NUs induce mitochondrial dysfunction, the caspase-3/PARP pathway activation, and cell damage through catalyzing a "$H_2O_2 \rightarrow O_2 \rightarrow {}^{\cdot}O_2^-$" successive reaction (Figure 2h).

**Biodegradation Ensured Safety Profiles of $MoO_{3-x}$ NUs.** Since the toxic $^{\cdot}O_2^-$ generation of $MoO_{3-x}$ NUs can be significantly inhibited in neutral solutions due to rapid biodegradation (Figures 1g and 2), the NUDPs are expected to be biocompatible and renal clearable (Figure

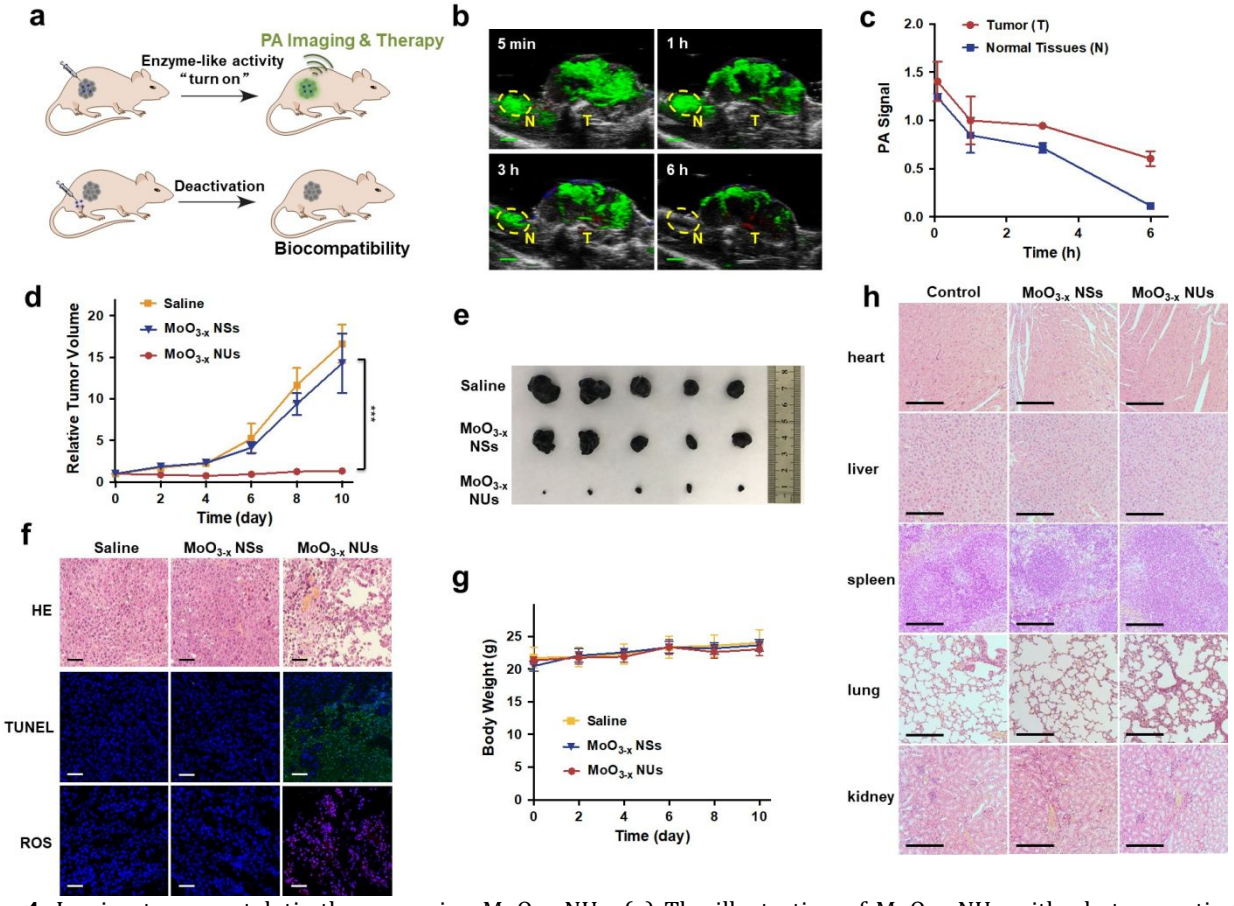


**Figure 4.** In vivo tumor catalytic therapy using $MoO_{3-x}$ NUs. (a) The illustration of $MoO_{3-x}$ NUs with photoacoustic (PA) signals and therapeutic activity in tumor regions, and their silencing in marginal normal tissues. (b) Merged ultrasound (US) and PA imaging of a BALB/c nude mouse harboring the B16 tumor xenograft at 5 min, 1 h, 3 h, and 6 h post in situ injection of $MoO_{3-x}$ NUs. T, tumor; N, normal tissue. Scale bar=2 mm. (c) The mean of highest PA signal values at various time points of corresponding PA imaging (b; λ=910 nm). (d,e) Tumor growth curves (d) and image of tumors (e) of BALB/c nude mice harboring the B16 tumor xenograft after different treatments (n=5). (f) Hematoxylin and eosin (HE) staining, terminal deoxynucleotidyl transferase dUTP nick end labeling (TUNEL) staining, and ROS staining of tumors after different treatments. Scale bar=50 μm. (g) Body weights of BALB/c nude mice harboring the B16 tumor xenograft during different treatments. (h) HE staining of various organs in BALB/c nude mice harboring the B16 tumor xenograft after different treatments. Scale bar=200 μm. *P<0.05, **P<0.01, ***P<0.001.

3a). The safety of $MoO_{3-x}$ NUs was investigated both in vitro and in vivo. We find that the NUDPs show negligible cytotoxicity to both tumor cells (Figure 3b) and normal cells (Figure 3c). Also, after intravenous injection, the majority of $MoO_{3-x}$ NUs are rapidly biodegraded into biocompatible NUDPs and then cleared from blood circulation by urinary excretion (Figure 3d), thus ensuring safety. Consequently, both hematological test results (Figure 3e) and blood biochemical test results (Figure 3f) show no obvious change after the treatment of $MoO_{3-x}$ NUs, indicating the $MoO_{3-x}$ NUs are highly biocompatible in vivo owing to the responsive biodegradation.

**In Vivo Tumor Specific Catalytic Activity of $MoO_{3-x}$ NUs.** As a localized surface plasmon resonance (LSPR) nanomaterial, $MoO_{3-x}$ NUs exhibit high photoacoustic (PA) signals in the 870-950 nm range,[33,50] which, however, become diminished after biodegradation (Figure S23). Therefore, we performed PA imaging to monitor the in vivo fate of $MoO_{3-x}$ NUs in the tumor and the adjacent normal tissue (Figure 4a). PA imaging was conducted at 5 min, 1 h, 3 h, and 6 h after in situ injection (Figure 4b). Interestingly, the PA signal intensity in the normal tissue displays a sharp time-dependent reduction and almost vanishes at 6 h post-injection. However, the PA signal intensity at the tumor site remains high for more than 6 h (Figure 4c). The slow decrease of PA signal in the tumor tissue is attributed to the consumption of $MoO_{3-x}$ NUs in the "$H_2O_2 \rightarrow O_2 \rightarrow {}^{\cdot}O_2^-$" cascade reaction. Moreover, the Mo levels in both tumor tissues and muscles were quantified by ICP-MS. As shown in Figure S24, the time-dependent decrease of Mo levels is consistent with PA results, owing to the loss of Mo ions following the consumption of $MoO_{3-x}$ NUs.[51] It implies that $MoO_{3-x}$ NUs can achieve long-term tumor retention, facilitating tumor imaging and therapy.

We further assessed the tumor therapeutic effect of $MoO_{3-x}$ NUs in vivo. As shown in Figure 4d,e, the tumor inhibition rate of $MoO_{3-x}$ NUs is as high as 92% after treatment. And it is worth mentioning that the mean relative tumor volume of the $MoO_{3-x}$ NUs-treated mice is 10.8-fold less than that of the $MoO_{3-x}$ NSs-treated mice.

Hematoxylin & eosin (HE) staining and terminal deoxynucleotidyl transferase dUTP nick end label (TUNEL) staining reveal a markedly higher apoptotic rate in the tumor tissue upon $MoO_{3-x}$ NUs treatment (Figure 4f). Furthermore, the ROS level in $MoO_{3-x}$ NUs-treated tumors is significantly higher than that in $MoO_{3-x}$ NSs-treated tumors, deriving from the in vivo $^{\cdot}O_2^-$ overproduction triggered by $MoO_{3-x}$ NUs. Moreover, body weights of mice (Figure 4g) and HE staining of various organs after treatment (Figure 4h), as well as the hematological and blood biochemical tests results after intramuscular injection (Figure S25) reveal no obvious toxicity of biodegradable $MoO_{3-x}$ NUs.

## CONCLUSION

In summary, we have developed a biodegradation-medicated in vivo catalytic activity tunable nanozyme, $MoO_{3-x}$ NUs, which not only precisely perform highly tumor-specific cascade catalytic therapy, but also leave normal tissues unharmed due to their rapid and responsive biodegradation under normal physiological conditions. In the acidic tumor microenvironment, $MoO_{3-x}$ NUs with the CAT-like activity and OXD-like activity mediate a "$H_2O_2 \rightarrow O_2 \rightarrow {}^{\cdot}O_2^-$" cascade reaction to cause tumor cells apoptosis and significantly inhibit the tumor growth. However, on exposure to the physiological environment (pH~7.4), $MoO_{3-x}$ NUs are easily oxidized and biodegraded into renal clearable ion species with the vanishment of enzymatic activity. We explored pH-responsive biodegradation-mediated structural regulation to fine-tune the enzymatic activity of $MoO_{3-x}$ NUs for tumor specific cascade catalytic therapy with minimal off-target toxicity. Therefore, harnessing the unique features and regulating the catalytic reactivities of engineered nanomaterials would facilitate the rational design of smart nanozymes to regulate their in vivo performances.

## EXPERIMENTAL SECTION

**Materials.** Molybdenyl acetylacetonate, hexadecylamine, 1-octadecene, 1,3-diphenylisobenzofuran (DPBF), 3,3',5,5'-tetramethylbenzidine (TMB) and methylene blue (MB) were purchased from Aladdin Industrial Inc. (Shanghai, China). 5-tertbutoxycarbonyl-5methyl-1-pyrroline N-oxide (BMPO) was purchased from APExBIO (Houston, USA). Oleic acid (90%) was purchased from Sigma-Aldrich Co. (St. Louis, MO, USA). Chloroform, cyclohexane, ethanol, hydrochloric acid (HCl), sodium hydroxide (NaOH), and hydrogen peroxide ($H_2O_2$) were purchased from Sinopharm Chemical Reagent Co., Ltd. (Shanghai, China). 1,2-distearoyl-sn-glycero-3-phosphoethanolamine-N-[methoxy (polyethylene glycol)-2000] (DSPE-$PEG_{2000}$) was obtained from Shanghai Advanced Vehicle Technology Pharmaceutical Co., Ltd. (Shanghai, China). Fetal bovine serum was obtained from Sijiqing Biologic Co., Ltd. (Hangzhou, China). Dulbecco's modified Eagle medium (DMEM) was obtained from Jinuo Biomedical Technology Co., Ltd. (Hangzhou, China). Cell Counting Kit-8, Reactive Oxygen Species Assay Kit (DCFH-DA), Mitochondrial Membrane Potential Assay Kit (JC-1), and Hoechst 33342 staining solution were purchased from Beyotime Biotechnology. (Shanghai, China).

**Synthesis of $MoO_{3-x}$ Nanourchins (NUs).** 40 mg of molybdenyl acetylacetonate, 0.20 g of hexadecylamine (HDA), and 2.0 mL of oleic acid (OA) were added to 8 mL of 1-octodecene, which were then uniformly heated at 100 °C for 10 min. The mixture (as a pre-heating product) was transferred into a Teflon-lined autoclave (15 mL), which was then maintained at 160 °C for 12 h. After centrifugation (11000 rpm, 10 min), the precipitate was washed three times with ethanol and finally dispersed in chloroform.

**Synthesis of $MoO_{3-x}$ Nanosheets (NSs).** In a typical procedure,[31] 0.5 g of ammonium molybdate was dissolved in 26 mL of deionized water and 2.4 mL of HCl (1 M). Then 1.6 g of oleylamine was dissolved in 8 mL of cyclohexane, and added into ammonium molybdate solution. The milky emulsion was then transferred into a Teflon-lined autoclave (50 mL) and maintained at 180 °C for 12 h. The blue $MoO_{3-x}$ NSs were extracted by adding cyclohexane and then precipitated by adding the double volume of ethanol. After centrifugation (11000 rpm, 10 min), the precipitate was washed three times with ethanol and finally dispersed in chloroform.

**Surface Modification of $MoO_{3-x}$ NUs and $MoO_{3-x}$ NSs.** DSPE-$PEG_{2000}$ was used to transform $MoO_{3-x}$ NUs or $MoO_{3-x}$ NSs into aqueous phase. Briefly, 20 mg of DSPE-$PEG_{2000}$ and 2 mg of $MoO_{3-x}$ NUs or $MoO_{3-x}$ NSs were mixed in chloroform under magnetic stirring. The dispersion was dried by rotary evaporation under vacuum for 1 h before adding distilled water. Excess surfactants were then removed by centrifugation.

**Preparation of $MoO_{3-x}$ NUs Degradation Products (NUDPs).** Complete degradation would be achieved by dispersing $MoO_{3-x}$ NUs in NaOH solution (1 M) at 60 °C for 24 h (Mo, 1 mg $mL^{-1}$). The NUDPs were then obtained after lyophilization.

**Characterization.** Transmission electron micrograph (TEM) images were taken using a HITACHI HT7700 at a voltage of 120 kV. Elemental analysis of $MoO_{3-x}$ NUs was studied using a FEI Tecnai G2 F20 S-TWIN field-emission microscope. The molybdenum element concentration was determined by a PerkinElmer NexION 300XX inductively coupled plasma mass spectrometer (ICP-MS). X-ray powder diffraction (XRD) pattern was collected on a X-pert Powder (PANalytical B.V., Holland). X-ray photoelectron spectroscopy (XPS) analysis was performed on a VG Scientific ESCALAB Mark II spectrometer. Raman spectrum was measured on a LabRAM HR Evolution (HORIBA France SAS, France). Dynamic light scattering (DLS) was conducted on a Zetasizer Nano ZS90 equipment (Malvern instruments, UK).

**The pH-Dependent Behavior of $MoO_{3-x}$ NUs.** After dispersing the $MoO_{3-x}$ NUs in PBS (pH 6.0, pH 7.4, and pH 8.5; 10 mM) or 1 mM $H_2O_2$/PBS (pH 6.0, 10 mM), the size, appearance, and UV-Vis-NIR absorption of $MoO_{3-x}$ NUs were studied at various time points. In addition, the Mo ion release was conducted after placing $MoO_{3-x}$ NUs (Mo, 80 μg) in a dialysis tube (MWCO 3500 Da) and dialyzing against 10 mL of PBS (pH 6.0, pH 7.4, and pH 8.5; 10 mM) or 1 mM $H_2O_2$/PBS (pH 6.0, 10 mM) at 37 °C. The release medium was all taken out and the same volume of fresh medium was added at various time points. The amount of released Mo was directly quantified using the ICP-MS.

**Catalase (CAT)-Like Activity.** 20 μL of $MoO_{3-x}$ NUs (1 mg $mL^{-1}$) and 1 μL of $H_2O_2$ (1 M) were added into 1 mL of PBS (pH 6.0, pH 7.4, and pH 8.5; 10 mM). After incubation at 40 °C, the CAT reactions were recorded by photography.

**Measurement of $O_2$ Production.** 240 μL of $MoO_{3-x}$ NUs (1 mg $mL^{-1}$) and 60 μL of $H_2O_2$ (1 M) were added into 6 mL of PBS (pH 6.0, pH 7.4, and pH 8.5; 10 mM), the oxygen generation ability was evaluated by an oxygen electrode on Dissolved Oxygen Meter JPB-607 (Shanghai INESA Scientific Instrument, China).

**Oxidase (OXD)-Like Activity.** 80 μL of $MoO_{3-x}$ NUs (1 mg $mL^{-1}$) or $MoO_{3-x}$ NSs (1 mg $mL^{-1}$), and 200 μL of OPD (50 mM) were added into HAc/NaAc buffer solution (pH 4.5, 0.1 M; the total volume of mixture is 2 mL) with or without 4 μL of $H_2O_2$ (1 M). The reaction was measured at certain time points by a UV-Vis spectroscopy at 450 nm. In addition, TMB (1 mM) was also employed to verify the OXD-like activity of $MoO_{3-x}$ NUs and $MoO_{3-x}$ NSs, and the reaction was measured at certain time points by a UV-Vis spectroscopy at 652 nm. After incubated with $H_2O_2$ (0.1 mM, 1 mM, and 10 mM) for 1 h or 1 mM $H_2O_2$ at different times (1 h, 3 h, and 6 h), $MoO_{3-x}$ NUs were collected by centrifugation (11000 rpm, 10 min) and washed by water to remove excess $H_2O_2$. Moreover, the residual $H_2O_2$ was measured using UV-Vis spectroscopy based on the starch-iodine complex. Briefly, 0, 0.20, 0.40, 0.60, 0.80 and 1.00 mL of $H_2O_2$ solution (10 μg $mL^{-1}$) was diluted to 5 mL using distilled water respectively, and 1.0 mL of HCl (10%), 0.5 mL of sodium chloride solution (200 mg $mL^{-1}$), 0.3 mL of potassium iodide solution (10 mg $mL^{-1}$) and 0.2 mL starch solution (10 mg $mL^{-1}$) were sequentially added. After incubation for 40 min, the absorbance was measured by a UV-Vis spectroscopy at 560 nm, and a standard curve in the range of 0-60 nmol $mL^{-1}$ was plotted with $H_2O_2$ concentration versus UV absorbance. The amount of residual $H_2O_2$ in $MoO_{3-x}$ NUs was measured directly using the standard curve. Furthermore, to study the OXD-like activity, 80 μL of $MoO_{3-x}$ NUs (1 mg $mL^{-1}$) and 200 μL of OPD (50 mM) were added into 2 mL of HAc/NaAc buffer solution (pH 4.5, 0.1 M). The absorbance of the OXD reaction was detected at a certain time by a UV-Vis spectroscopy at 450 nm.

**ESR measurements.** For $^{\cdot}O_2^-$ detection, the PBS (pH 5.0, 25 mM) containing BMPO (25 mM), $H_2O_2$ (1 mM), and $MoO_{3-x}$ NUs or $MoO_{3-x}$ NSs (20 μg $mL^{-1}$) was prepared. ESR spectra were recorded after 3 min incubation.

**In Vitro $^{\cdot}O_2^-$ Detection.** DPBF was used to detect the in vitro generation of ROS including $^{\cdot}O_2^-$ and $^1O_2$. 20 μL of DPBF ethanol solution (10 mM), 1 μL of $H_2O_2$ solution (2 M), and 20 μL of $MoO_{3-x}$ NUs (1 mg $mL^{-1}$) were dispersed in the mixed solution ($V_{ethanol}$:$V_{water}$=6:4) with a total volume of 2 mL. The generation of $^{\cdot}O_2^-$ was measured at different times (0, 2, 5, 10, 20, and 30 min) by a UV-Vis spectroscopy at 410 nm. Furthermore, excess superoxide dismutase (a $^{\cdot}O_2^-$ scavenger) or carotene (a $^1O_2$ scavenger) was added into this system to investigate the specific kind of ROS. The particle size and the generation of $^{\cdot}O_2^-$ were detected after the storage of $MoO_{3-x}$ NUs in distilled water for 1 d, 3 d, 5 d and 7 d. Moreover, to study the reusability of $MoO_{3-x}$ NUs, the $^{\cdot}O_2^-$ generation was detected by UV-Vis spectroscopy at 410 nm after adding the same amount of $H_2O_2$ and DPBF into a $MoO_{3-x}$ NUs sample for three times.

**In Vitro ·OH Detection.** 20 μL of $MoO_{3-x}$ NUs (1 mg $mL^{-1}$) or 20 μL of $MoO_{3-x}$ NSs (1 mg $mL^{-1}$), and 1 μL of $H_2O_2$ (2 M) were added in 3 mL of MB solution (8 μg $mL^{-1}$). The generation of ·OH was measured at different time points (0, 2, 5, 10, 20, and 30 min) by a UV-Vis spectroscopy at 663 nm.

**Cellular Uptake.** After surface modification, 0.25 mL of $MoO_{3-x}$ NUs (1 mg $mL^{-1}$) or $MoO_{3-x}$ NSs (1 mg $mL^{-1}$) was mixed with 0.25 mL of FITC ethanol solution (10 mg $mL^{-1}$). After stirring in the dark for 6 h, $MoO_{3-x}$ NUs/FITC or $MoO_{3-x}$ NSs/FITC were washed three times with 50% ethanol solution via centrifugation (10000 rpm, 10 min) to remove free FITC. After washed with PBS (pH 6.0) and DMEM (pH 6.0), $MoO_{3-x}$ NUs/FITC or $MoO_{3-x}$ NSs/FITC were dispersed in DMEM (pH 6.0). B16 melanoma cells were cultured in DMEM supplemented with 10% fetal bovine serum at 37 °C in an atmosphere containing 5% $CO_2$. B16 cells were seeded on confocal dishes with a glass-bottom insert (Wuxi NEST Biotechnology Co., Ltd, China) and incubated for 12 h. And then the DMEM was replaced with fresh DMEM (pH 6.0) containing $MoO_{3-x}$ NUs/FITC (Mo, 6.25 μg $mL^{-1}$) or $MoO_{3-x}$ NSs/FITC (Mo, 6.25 μg $mL^{-1}$). After incubation at 37 °C for 1 h and 4 h, the cells were washed for 3 times with PBS and fixed with 4% paraformaldehyde solution for 30 min. DAPI (dilution 1:20) was then used to visualize the nuclei. Cells were observed by a confocal laser scanning microscope (CLSM; Olympus FV1000, Japan) to confirm the cellular uptake.

**Intracellular ROS Detection.** The ROS was detected using 2', 7'-dichlorofluorescein-diacetate (DCFH-DA). B16 cells were seeded on confocal dishes with a glass-bottom insert (Wuxi NEST Biotechnology Co., Ltd, China) and incubated for 12 h. And then the DMEM was replaced with fresh DMEM (pH 6.0 or pH 7.4) containing $MoO_{3-x}$ NUs (6.25 μg $mL^{-1}$) or $MoO_{3-x}$ NSs (6.25 μg $mL^{-1}$), respectively. After 12 h, the cells were washed and incubated in DCFH-DA working solution (10 μM) at 37 °C for 20 min. The cells were washed with PBS for three times and observed using a CLSM (Olympus FV1000, Japan).

**JC-1 Staining.** B16 cells were seeded on confocal dishes with a glass-bottom insert (Wuxi NEST Biotechnology Co., Ltd, China) and incubated for 12 h. And then the DMEM was replaced with fresh DMEM (pH 6.0 or pH 7.4) containing $MoO_{3-x}$ NUs (6.25 μg $mL^{-1}$) or $MoO_{3-x}$ NSs (6.25 μg $mL^{-1}$), respectively. After 12 h, the cells were washed and incubated in JC-1 working solution at 37 °C for 20 min. The cells were washed with PBS for three times and incubated in Hoechst 33342 solution at 37 °C for 10 min. The cells were washed with PBS for three times, and observed using a CLSM (Olympus IX83-FV3000-OSR, Japan).

**Cell Viability Assay.** B16 cells or L02 normal liver cells ($10^4$ cells $well^{-1}$) were seeded in 96 well plates with 200 μL culture medium. After 12 h, cells were treated with DMEM (pH 6.0 or pH 7.4) containing various concentrations of $MoO_{3-x}$ NUs (0, 1.56, 3.125, 6.25, and 12.5 μg $mL^{-1}$) for 24 h, respectively. The medium was replaced with 200 μL of 10% CCK-8/DMEM solution. After incubation for another 4 h, the absorbance of each well was measured at 450 nm with a microplate reader (ELx800, Bio Tek Instruments Inc., USA). In addition, the cell viability after treatment with NUDPs was also evaluated by the same procedure.

**Western Blotting.** B16 cells were cultured in DMEM (pH 6.0 or pH 7.4) containing $MoO_{3-x}$ NUs (6.25 μg $mL^{-1}$) or $MoO_{3-x}$ NSs (6.25 μg $mL^{-1}$), respectively. After 12 h, B16 cells were collected and lysed in universal lysis buffer (50 mM Tris-HCl, 150 mM NaCl, 2 mM EDTA, 2 mM EGTA, 25 mM NaF, 25 mM β-glycerophosphate pH 7.5, 0.1 mM sodium orthovanadate, 0.1 mM PMSF, 5 μg of leupeptin $mL^{-1}$, 0.2% Triton X-100, 0.5% Nonidet P-40). Protein concentrations were further determined with the Lowry protein assay. The proteins were separated by SDS-PAGE and transferred to PVDF membranes (IPVH00010, Millipore, Billerica, Massachusetts, USA) and probed with primary antibodies. The primary antibodies were listed as follows: cleaved PARP (1:1000, mouse specific, 9544S), cleaved caspase 3 (1:1000, 9661L) from Cell Signaling Technology (Danvers, Massachusetts, USA); Bcl-2 (1:1000, sc-7382), Bax (1:1000, sc-7480), β-Actin (1:1000, sc-1615) from Santa Cruz Biotechnology (Dallas, USA). Corresponding secondary antibodies (MultiSciences, Hangzhou, China) and ECL (NEL105001EA, PerkinElmer, Ohio, USA) were further incubated to detect enhanced chemiluminescence.

**In Vitro and in Vivo Photoacoustic (PA) Imaging.** PA signals of $MoO_{3-x}$ NUs and the corresponding NUDPs (2 mg $mL^{-1}$) at the range from 680 nm to 970 nm were recorded using a Vevo LAZR instrument (Fujifilm, Canada). Then, $MoO_{3-x}$ NUs (10 mg $kg^{-1}$) were injected into the tumor site and adjacent normal tissue of a BALB/c nude mouse harboring the B16 tumor xenograft. The PA imaging of the BALB/c nude mouse harboring the B16 tumor xenograft was recorded at 5 min, 1 h, 3 h, and 6 h post-injection of $MoO_{3-x}$ NUs at 910 nm using a Vevo LAZR instrument (Fujifilm, Canada). In addition, both tumor and muscle were harvested at 5 min, 1 h, 3 h, and 6 h post-injection of $MoO_{3-x}$ NUs, and digested overnight in 5 mL $HNO_3$ at 60 °C. After dilution and filtration through a 0.22 μm filter, the Mo levels in sample solutions were quantified by using ICP-MS.

**In Vivo Anti-Tumor Treatment.** $5\times10^6$ B16 tumor cells were injected to the back of male BALB/c nude mice. After a week, the BALB/c nude mice harboring a B16 tumor xenograft were randomly divided into three groups (n=5), and were intratumorally injected with PBS, $MoO_{3-x}$ NUs (10 mg $kg^{-1}$), and $MoO_{3-x}$ NSs (10 mg $kg^{-1}$) every 3 days, respectively. Tumor volumes (tumor volume=width$^2$×length/2) and body weights were measured every 2 days. At the end of treatments, tumors and various organs (heart, liver, spleen, lung, and kidney) were harvested for staining (Tumor: hematoxylin & eosin (HE) staining, terminal deoxynucleotidyl transferase dUTP nick end label (TUNEL), and ROS staining; Organs: HE staining). Animal experiments were carried out according to institutional guidelines and were approved by Zhejiang University Laboratory Animal Center.

**Hematological and Blood Biochemical Tests.** BALB/c mice were intravenously or intramuscularly injected with $MoO_{3-x}$ NUs (5 mg $kg^{-1}$) to study the tissue toxicity caused by the possible leakage (n=6). Hematological and blood biochemical tests were performed at 0 d, 2 d, and 7 d post-injection.

## ASSOCIATED CONTENT

### Supporting Information

The Supporting Information is available free of charge on the ACS Publications website at http://pubs.acs.org.

## AUTHOR INFORMATION

### Corresponding Author

* lingds@zju.edu.cn

### Author Contributions

D. L., X. H. and F. L. conceived and designed the study. X. H., F. L., F. X., X. G., N. W. and L. L. performed the experiments. X. H., F. L., F. X., X. G. and L. L. synthesized the materials and detected enzymatic activity. X. H., F. X. and N. W. performed the cell and animal experiments. D.L., X. H., F. L. and F. X. analyzed the data and wrote the manuscript. D.L., F.L., B. Y., K. F. and X. Y. provided project supervision. All the authors discussed the results and approved the final version of the manuscript.

### Notes

The authors declare no competing financial interest.

## ACKNOWLEDGMENT

We acknowledge financial support by National Key Research and Development Program of China (2016YFA0203600), the National Natural Science Foundation of China (31822019, 51703195, 91859116), "Thousand Talents Program" for Distinguished Young Scholars, the One Belt and One Road International Cooperation Project from Key Research and Development Program of Zhejiang Province (2019C04024), the Zhejiang Provincial Natural Science Foundation of China (LGF19C100002), the Fundamental Research Funds for the Central Universities (2018QNA7020), and Zhejiang Pharmaceutical Association (2019ZYY12).

## REFERENCES

(1) Huo, M.; Wang, L.; Chen, Y.; Shi, J. Tumor-selective catalytic nanomedicine by nanocatalyst delivery. *Nat. Commun.* **2017,** *8,* 357.

(2) Wang, Z.; Zhang, Y.; Ju, E.; Liu, Z.; Cao, F.; Chen, Z.; Ren, J.; Qu, X. Biomimetic nanoflowers by self-assembly of nanozymes to induce intracellular oxidative damage against hypoxic tumors. *Nat. Commun.* **2018,** *9,* 3334.

(3) Fan, K.; Xi, J.; Lei, F.; Wang, P.; Zhu, C.; Yan, T.; Xu, X.; Liang, M.; Bing, J.; Yan, X.; Gao, L. In vivo guiding nitrogen-doped carbon nanozyme for tumor catalytic therapy. *Nat. Commun.* **2018,** *9,* 1440.

(4) Lin, L. S.; Song, J.; Song, L.; Ke, K.; Liu, Y.; Zhou, Z.; Shen, Z.; Li, J.; Yang, Z.; Tang, W.; Niu, G.; Yang, H.; Chen, X. Simultaneous fenton-like ion delivery and glutathione depletion by $MnO_2$-based nanoagent to enhance chemodynamic therapy. *Angew. Chem. Int. Ed.* **2018,** *57,* 4902-4906.

(5) Natalio, F.; André, R.; Hartog, A. F.; Stoll, B.; Jochum, K. P.; Wever, R.; Tremel, W. Vanadium pentoxide nanoparticles mimic vanadium haloperoxidases and thwart biofilm formation. *Nat. Nanotechnol.* **2012,** *7,* 530-535.

(6) Sun, H.; Zhou, Y.; Ren, J.; Qu, X. Carbon nanozymes: enzymatic properties, catalytic mechanism, and applications. *Angew. Chem. Int. Ed.* **2018,** *57,* 9224-9237.

(7) Xia, H.; Li, F.; Hu, X.; Park, W.; Wang, S.; Jang, Y.; Du, Y.; Baik, S.; Cho, S.; Taegyu, K.; Kim, D. H.; Ling, D.; Hui, K. M.; Hyeon, T. pH-sensitive Pt nanocluster assembly overcomes cisplatin resistance and heterogeneous stemness of hepatocellular carcinoma. *ACS Cent. Sci.* **2016,** *2,* 802-811.

(8) Hu, S.; Yi, T.; Huang, Z.; Liu, B.; Wang, J.; Yi, X.; Liu, J. Etching silver nanoparticles using DNA. *Mater. Horiz.* **2019**, *2,* 155-159.
(9) Du, J.; Gu, Z.; Yan, L.; Yong, Y.; Yi, X.; Zhang, X.; Liu, J.; Wu, R.; Ge, C.; Chen, C.; Zhao, Y. Poly(vinylpyrollidone)- and selenocysteine-modified $Bi_2Se_3$ nanoparticles enhance radiotherapy efficacy in tumors and promote radioprotection in normal tissues. *Adv. Mater.* **2017,** *29,* 1701268.
(10) Wu, J.; Wang, X.; Wang, Q.; Lou, Z.; Li, S.; Zhu, Y.; Qin, L.; Wei, H. Nanomaterials with enzyme-like characteristics (nanozymes): next-generation artificial enzymes (II). *Chem. Soc. Rev.* **2018,** *48,* 1004-1076.
(11) Wei, H.; Wang, E. Nanomaterials with enzyme-like characteristics (nanozymes): next-generation artificial enzymes. *Chem. Soc. Rev.* **2013,** *42,* 6060-6093.
(12) Huang, Y.; Ren, J.; Qu, X. Nanozymes: Classification, Catalytic mechanisms, activity regulation, and applications. *Chem. Rev.* **2019,** *119,* 4357-4412.
(13) Ragg, R.; Tahir, M. N.; Termel, W. Solids Go Bio: Inorganic nanoparticles as enzyme mimics. *Eur. J. Inorg. Chem.* **2016,** *2016,* 1906-1915.
(14) Zhang, Z.; Zhang, X.; Liu, X.; Liu, J. Molecular imprinting on inorganic nanozymes for hundred-fold enzyme specificity. *J. Am. Chem. Soc.* **2017,** *139,* 5412-5419.
(15) Ding, H.; Cai, Y.; Gao, L.; Liang, M.; Miao, B.; Wu, H.; Liu, Y.; Xie, N.; Tang, A.; Fan, K.; Yan, X.; Nie, G. Exosome-like nanozyme vesicles for $H_2O_2$-responsive catalytic photoacoustic imaging of xenograft nasopharyngeal carcinoma. *Nano Lett.* **2019,** *19,* 203-209.
(16) Wang, X.; Gao, X. J.; Qin, L.; Wang, C.; Song, L.; Zhou, Y.; Zhu, G.; Cao, W.; Lin, S.; Zhou, L.; Wang, K.; Zhang, H.; Jin, Z.; Wang, P.; Gao, X.; Wei, H. $e_g$ occupancy as an effective descriptor for the catalytic activity of perovskite oxide-based peroxidase mimics. *Nat. Commun.* **2019,** *10,* 704.
(17) Zhang, J.; Wu, S.; Lu, X.; Wu, P.; Liu, J. Manganese as a catalytic mediator for photo-oxidation and breaking the pH limitation of nanozymes. *Nano Lett.* **2019,** *19,* 3214-3220.
(18) André, R.; Natálio, F.; Humanes, M.; Leppin, J.; Heinze, K.; Wever, R.; Schröder, H. C.; Müller, W. E. G.; Tremel, W. $V_2O_5$ nanowires with an intrinsic peroxidase-like activity. *Adv. Funct. Mater.* **2011,** *21,* 501-509.
(19) Cheng, Z.; Zaki, A. A.; Hui, J. Z.; Muzykantov, V. R.; Tsourkas, A. Multifunctional nanoparticles: cost versus benefit of adding targeting and imaging capabilities. *Science* **2012,** *338,* 903-910.
(20) Tibbitt, M. W.; Dahlman, J. E.; Langer, R. Emerging frontiers in drug delivery. *J. Am. Chem. Soc.* **2016,** *138,* 704-717.
(21) Hermann, J. C.; Marti-Arbona, R.; Fedorov, A. A.; Fedorov, E.; Almo, S. C.; Shoichet, B. K.; Raushel, F. M. Structure-based activity prediction for an enzyme of unknown function. *Nature* **2007**, *448,* 775-779.
(22) Romanski, S.; Stamellou, E.; Jaraba, J. T.; Storz, D.; Krämer, B. K.; Hafner, M.; Amslinger, S.; Schmalz, H. G.; Yard, B. A. Enzyme-triggered CO-releasing molecules (ET-CORMs): evaluation of biological activity in relation to their structure. *Free Radical Bio. Med.* **2013,** *65,* 78.
(23) Sheehy, A. M.; Gaddis, N. C.; Malim, M. H. The antiretroviral enzyme APOBEC3G is degraded by the proteasome in response to HIV-1 Vif. *Nat. Med.* **2003,** *9,* 1404-1407.
(24) Ye, E.; Regulacio, M. D.; Zhang, S. Y.; Loh, X. J.; Han, M. Y. Anisotropically branched metal nanostructures. *Chem. Soc. Rev.* **2015,** *44,* 6001-6017.
(25) Narayanan, R.; Tabor, C.; El-Sayed, M. A. Can the observed changes in the size or shape of a colloidal nanocatalyst reveal the nanocatalysis mechanism type: Homogeneous or heterogeneous? *Top. Catal.* **2008,** 48, 60-74.
(26) Ma, L.; Wang, C.; Gong, M.; Liao, L.; Long, R.; Wang, J.; Wu, D.; Zhong, W.; Kim, M. J.; Chen, Y.; Xie, Y.; Xiong, Y. Control over the branched structures of platinum nanocrystals for electrocatalytic applications. *ACS Nano* **2012,** *6,* 9797-9806.
(27) Singh, N.; Savanur, M. A.; Srivastava, S.; D'Silva, P.; Mugesh, G. A redox modulatory $Mn_3O_4$ nanozyme with multi-enzyme activity provides efficient cytoprotection to human cells in a Parkinson's disease model. *Angew. Chem. Int. Ed.* **2017,** *56,* 14267-14271.
(28) Li, Y.; Cheng, J.; Li, J.; Zhu, X.; He, T.; Chen, R.; Tang, Z. Tunable chiroptical properties from the plasmonic band to metal-ligand charge transfer band of cysteine-capped molybdenum oxide nanoparticles. *Angew. Chem. Int. Ed.* **2018,** *57,* 10236-10240.
(29) Borgschulte, A.; Sambalova, O.; Delmelle, R.; Jenatsch, S.; Hany, R.; Nüesch, F. Hydrogen reduction of molybdenum oxide at room temperature. *Sci. Rep.* **2017,** *7,* 40761.
(30) Tang, W.; Fan, W.; Wang, Z.; Zhang, W.; Zhou, S.; Liu, Y.; Yang, Z.; Shao, E.; Zhang, G.; Jacobson, O.; Shan, L.; Tian, R; Cheng, S.; Lin, L.; Dai, Y.; Shen, Z.; Niu, G.; Xie, J.; Chen, X. Acidity/reducibility dual-responsive hollow mesoporous organosilica nanoplatforms for tumor-specific self-assembly and synergistic therapy. *ACS Nano* **2018,** *12,* 12269-12283.
(31) Song, G.; Hao, J.; Liang, C.; Liu, T.; Gao, M.; Cheng, L.; Hu, J.; Liu, Z. Degradable molybdenum oxide nanosheets with rapid clearance and efficient tumor homing capabilities as a therapeutic nanoplatform. *Angew. Chem. Int. Ed.* **2016,** *55,* 2122-2126.
(32) Zhang, C.; Bu, W.; Ni, D.; Zuo, C.; Cheng, C.; Li, Q.; Zhang, L.; Wang, Z.; Shi, J. A polyoxometalate cluster paradigm with self-adaptive electronic structure for acidity/reducibility-specific photothermal conversion. *J. Am. Chem. Soc.* **2016,** *138,* 8156-8164.
(33) Song, G.; Shen, J.; Jiang, F.; Hu, R.; Li, W.; An, L.; Zou, R.; Chen, Z.; Qin, Z.; Hu, J. Hydrophilic molybdenum oxide nanomaterials with controlled morphology and strong plasmonic absorption for photothermal ablation of cancer cells. *ACS Appl. Mater. Interfaces* **2014,** *6,* 3915-3922.
(34) Jin, M.; He, G.; Zhang, H.; Zeng, J.; Xie, Z.; Xia, Y. Shape-controlled synthesis of copper nanocrystals in an aqueous solution with glucose as a reducing agent and hexadecylamine as a capping agent. *Angew. Chem. Int. Ed.* **2011,** *50,* 10560-10564.
(35) Liu, Q.; Guo, X.; Li, Y.; Shen, W. Synthesis of hollow Co structures with netlike framework. *Langmuir* **2009,** *25,* 6425-6430.
(36) Gong, F.; Cheng, L.; Yang, N.; Jin, Q.; Tian, L.; Wang, M.; Li, Y.; Liu, Z. Bimetallic oxide $MnMoO_x$ nanorods for in vivo photoacoustic imaging of GSH and tumor-specific photothermal therapy. *Nano Lett.* **2018,** *18,* 6037-6044.
(37) Ni, D.; Jiang, D.; Valdovinos, H. F.; Ehlerding, E. B.; Yu, B.; Barnhart, T. E.; Huang, P.; Cai, W. Bioresponsive polyoxometalate cluster for redox-activated photoacoustic imaging-guided photothermal cancer therapy. *Nano Lett.* **2017,** *17,* 3282-3289.
(38) Liu, W.; Li, X.; Li, W.; Zhang, Q.; Bai, H.; Li, J.; Xi, G. Highly stable molybdenum dioxide nanoparticles with strong plasmon resonance are promising in photothermal cancer therapy. *Biomaterials* **2018,** *163,* 43-54.
(39) Long, R.; Mao, K.; Ye, X.; Yan, W.; Huang, Y.; Wang, J.; Fu, Y.; Wang, X.; Wu, X.; Xie, Y.; Xiong, Y. Surface facet of palladium nanocrystals: a key parameter to the activation of molecular oxygen for organic catalysis and cancer treatment. *J. Am. Chem. Soc.* **2013,** *135,* 3200-3207.
(40) Castro, I. A.; Datta, R. S.; Ou, J. Z.; Castellanos-Gomez, A.; Sriram, S.; Daeneke, T.; Kalantar-zadeh, K. Molybdenum oxides-from fundamentals to functionality. *Adv. Mater.* **2017,** *29,* 1701619.
(41) Ni, D.; Jiang, D.; Kutyreff, C. J.; Lai, J.; Yan, Y.; Barnhart, T. E.; Yu, B.; Im, H.-J.; Kang, L.; Cho, S. Y.; Liu, Z.; Huang, P.; Engle, J. W.; Cai, W. Molybdenum-based nanoclusters act as antioxidants and ameliorate acute kidney injury in mice. *Nat. Commun.* **2018,** *9,* 5421.
(42) Kuwahara, Y.; Yoshimura, Y.; Haematsu, K.; Yamashita, H. Mild deoxygenation of sulfoxides over plasmonic molybdenum oxide hybrid with dramatic activity enhancement under visible light. *J. Am. Chem. Soc.* **2018,** *140,* 9203-9210.
(43) Ragg, R.; Natalio, F.; Tahir, M. N.; Janssen, H.; Kashyap, A.; Strand, D.; Strand, S.; Tremel, W. Molybdenum trioxide nanoparticles with intrinsic sulfite oxidase activity. *ACS Nano* **2014,** *8,* 5182-5189.
(44) Narayanan, R.; El-Sayed, M. A. Shape-dependent catalytic activity of platinum nanoparticles in colloidal solution. *Nano Lett.* **2004,** *4,* 1343-1348.
(45) Cuenya, B. R.; Behafarid, F. Nanocatalysis: size- and shape-dependent chemisorption and catalytic reactivity. *Surf. Sci. Rep.* **2015,** *70,* 135-187.

(46) Szatrowski, T. P.; Nathan, C. F. Production of large amounts of hydrogen peroxide by human tumor cells. *Cancer Res.* **1991,** *51,* 794-798.
(47) Pan, L.; Liu, J.; Shi, J. Intranuclear photosensitizer delivery and photosensitization for enhanced photodynamic therapy with ultralow irradiance. *Adv. Funct. Mater.* **2014,** *24,* 7318-7327.
(48) Nathan, C.; Cunningham-Bussel, A. Beyond oxidative stress: an immunologist's guide to reactive oxygen species. *Nat. Rev. Immunol.* **2013,** *13,* 349-361.
(49) Gorrini, C.; Harris, I. S.; Mak, T. W. Modulation of oxidative stress as an anticancer strategy. *Nat. Rev. Drug Discov.* **2013,** *12,* 931-947.
(50) Bao, T.; Yin, W.; Zheng, X.; Zhang, X.; Yu, J.; Dong, X.; Yong, Y.; Gao, F.; Yan, L.; Gu, Z.; Zhao, Y. One-pot synthesis of PEGylated plasmonic $MoO_{(3-x)}$ hollow nanospheres for photoacoustic imaging guided chemo-photothermal combinational therapy of cancer. *Biomaterials* **2016,** 76, 11-24.
(51) Yang, S.; Sun, S.; Zhou, C.; Hao, G.; Liu, J.; Ramezani, S.; Yu, M.; Sun, X.; Zheng, J. Renal clearance and degradation of glutathione-coated copper nanoparticles. *Bioconjugate Chem.* **2015**, *26*, 511-519.

**SYNOPSIS TOC**